



A multi-year survey of dynamics near the surface in the northern hemisphere of Mars: Short-period baroclinic waves and dust storms

David P. Hinson^{a,b,*}, Huiqun Wang^c, Michael D. Smith^d

^a Carl Sagan Center, SETI Institute, 189 Bernardo Ave., Mountain View, CA 94043, USA

^b Department of Electrical Engineering, Stanford University, 350 Serra Mall, Stanford, CA 94305, USA

^c Atomic and Molecular Physics Division, Smithsonian Astrophysical Observatory, 60 Garden St., Cambridge, MA 02138, USA

^d Planetary Systems Laboratory, NASA Goddard Space Flight Center, Greenbelt, MD 20771, USA

ARTICLE INFO

Article history:

Received 21 June 2011

Revised 10 February 2012

Accepted 4 March 2012

Available online 17 March 2012

Keywords:

Mars, Atmosphere

Mars, Climate

Atmospheres, Dynamics

Meteorology

ABSTRACT

Baroclinic waves figure prominently in the dynamics of the northern hemisphere of Mars, and extensive observations by the Viking Landers and two atmospheric sounders on Mars Global Surveyor have revealed many of their basic properties. However, previous investigations considered these data sets individually, so that their cumulative value is not fully appreciated. We have re-examined these data to extract new information about the dynamics near the surface at mid-to-high northern latitudes. By applying the same method of spectral analysis to each type of observation, we derive a uniform, multi-year characterization of basic elements of martian weather. This survey documents the time evolution of baroclinic waves among modes with different periods and zonal wave numbers. We devote particular attention to a recurring “wave-3 mode”, which is distinguished by its capacity to initiate regional dust storms in the topographic basins of the northern hemisphere. Our results include a detailed case study that shows how the intermittence of this mode and the strong zonal modulation of its amplitude influence the timing and location of these distinctive “flushing” dust storms. More generally, we find that the properties of the wave-3 mode are largely the same whenever it appears and that its intermittence plays an important role in the annual dust cycle.

© 2012 Elsevier Inc. All rights reserved.

1. Introduction

We are investigating atmospheric dynamics near the surface of Mars through reanalysis and intercomparison of an assortment of observations. The data sets considered here include surface pressures measured by the Viking Landers (VL) (e.g., Ryan et al., 1978; Zurek et al., 1992), wide-angle images acquired by the Mars Orbiter Camera (MOC) on Mars Global Surveyor (MGS) (e.g., Malin and Edgett, 2001; Cantor et al., 2001), and atmospheric profiles obtained by MGS through two techniques: infrared sounding by the Thermal Emission Spectrometer (TES) (e.g., Smith, 2004) and radio occultation sounding by the Radio Science (RS) facility instrument (e.g., Hinson et al., 1999). We restrict attention to the northern hemisphere, where the observations cover several more martian years than in the south.

The immediate goal of this investigation is a deeper understanding of the relationship between baroclinic waves and regional dust storms in the topographic basins of the northern hemisphere, which play a prominent role in the annual dust cycle. A careful

reanalysis of the VL and MGS observations allows us to gain new insight while consolidating and corroborating the results derived in many previous investigations. In addressing this topic, we will restrict attention to atmospheric dynamics within a few kilometers of the surface at latitudes of 50–70°N.

Although the objectives of this study can be addressed by “zooming in” on a narrow region of the atmosphere, the resulting discussion of atmospheric waves is neither balanced nor complete. A far different approach was adopted previously by Banfield et al. (2003, 2004), who derived comprehensive global maps of the spatial structure and seasonal evolution of a variety of atmospheric waves through extensive analysis of TES nadir temperature measurements. Their results cover the full altitude range of the TES retrievals, about 0–40 km, and extend from pole to pole, providing both context and guidance for more detailed investigations, such as the one described in this paper.

Our understanding of the basic properties and climatic significance of baroclinic waves on Mars has grown steadily over the past few decades. These advances originate primarily from analyses of the VL, TES, and RS observations (e.g., Ryan et al., 1978; Barnes, 1980, 1981; Leovy et al., 1985; Zurek et al., 1992; Collins et al., 1996; Hinson and Wilson, 2002; Wilson et al., 2002; Banfield et al., 2004; Wang et al., 2005; Hinson, 2006; Wang,

* Corresponding author at: Carl Sagan Center, SETI Institute, 189 Bernardo Ave., Mountain View, CA 94043, USA.

E-mail address: dhinson@seti.org (D.P. Hinson).

2007; Hinson and Wang, 2010). However, each investigation is limited in scope, whether by restricting attention to data from a single instrument, by considering a limited time span, or by using an approach that highlights some phenomena at the expense of others. Moreover, different methods of analysis have been applied to the VL, TES, and RS observations, and the results have been displayed in dissimilar formats. Important clues about the weather on Mars remain concealed within the three data sets.

Our investigation is designed to address these limitations. We exploit a combination of VL, TES, and RS data that spans many years. The complete set of observations has not been considered previously in any single publication. Moreover, we apply the same method of spectral analysis to all data sets, yielding the first uniform characterization of the baroclinic waves observed by these disparate instruments. This approach facilitates detailed comparisons among observations from different instruments and years, which allows several basic patterns of behavior to be identified clearly.

Before proceeding, we review the conventions for time keeping on Mars. The term “sol” denotes the mean solar day of 88,775 s. Local time is expressed in true solar hours (24 per sol). The areocentric longitude of the Sun L_s measures the seasons on Mars, with $L_s \equiv 0^\circ$ at the vernal equinox of the northern hemisphere. In assigning numbers to years we adopt the convention that Mars year 1 (MY 1) began on 11 April 1955 (Clancy et al., 2000).

The paper is organized as follows. Section 2 summarizes the basic properties of baroclinic waves in the northern hemisphere of Mars, consolidating results derived from previous analyses of the VL and MGS observations. After introducing our method of spectral analysis, we apply it to a subset of VL pressure data that exhibits distinctive “baroclinic wave transitions” among modes with different basic properties.

Section 3 explains how our method of spectral analysis is applied to the TES and RS observations, which directly sample both the spatial and temporal variations of the baroclinic waves. We use a pair of numerical simulations to characterize the method of analysis and the information content of the two data sets.

Section 4 illustrates the central themes of this investigation with a case study. We closely examine a subset of TES, RS, and MOC observations from midwinter of MY 25, yielding a detailed description of a weather pattern that appears intermittently at mid-to-high northern latitudes and strongly influences the timing and location of regional dust storms in the northern hemisphere. The central element of this weather pattern is an intense, short-period baroclinic wave with zonal wave number $s = 3$.

Section 5 reports analogous results derived from a broad survey of VL, TES, and RS data that collectively span ~ 7 MY. We show that the basic properties of the $s = 3$ baroclinic wave are largely the same whenever it appears, that it dominates the dynamics near the surface only within restricted intervals, which fall within two well-defined seasonal windows, and that its intermittence plays a decisive role in the annual dust cycle.

Section 6 describes possible directions for future research.

Color versions of Figs. 2, 3, 6–12, 15, 17, and 18 can be found in the web version of this article.

2. Basic properties of baroclinic waves

The numerous achievements of the two Viking Landers (henceforth VL1 and VL2) include the discovery of baroclinic waves in the northern hemisphere of Mars (e.g., Ryan et al., 1978; Barnes, 1980, 1981; Leovy et al., 1985; Zurek et al., 1992; Collins et al., 1996). Further observations of these martian weather systems were acquired by the atmospheric sounders on MGS (e.g., Wilson et al., 2002; Barnes, 2003; Banfield et al., 2004; Wang et al.,

2005; Hinson, 2006; Wang, 2007; Hinson and Wang, 2010). These disturbances reside in a baroclinic zone at mid-to-high northern latitudes, which is characterized by a steep meridional temperature gradient and strong eastward zonal winds (e.g., Banfield et al., 2003, 2004; Wang, 2007).

This section begins with a brief review of the basic properties of baroclinic waves in the northern hemisphere. We then use pressure data from VL2 to illustrate important aspects of their behavior. This information provides a context for more detailed discussions in subsequent sections.

2.1. Overview

Between late summer and early spring, an assortment of baroclinic waves appears at mid-to-high latitudes in the northern hemisphere and dominates the dynamics near the surface (e.g., Ryan et al., 1978; Barnes, 1980, 1981; Leovy et al., 1985; Zurek et al., 1992; Collins et al., 1996; Banfield et al., 2004; Wang et al., 2005; Hinson, 2006; Wang, 2007; Hinson and Wang, 2010). These eastward traveling waves are highly coherent, producing very regular oscillations in surface pressure, and their periodicity in longitude allows distinct modes to be classified according to their zonal wave number s (e.g., Banfield et al., 2004; Wang et al., 2005; Hinson, 2006; Wang, 2007; Hinson and Wang, 2010). In most cases the observed distribution of the baroclinic waves is trimodal, with $s = 1$ –3. The period of oscillation is shortest at $s = 3$ (2–3 sols) and longest at $s = 1$ (generally >6 sols). The amplitudes of the various modes are often anticorrelated—when one mode is strong the others are weak or absent (e.g., Fig. 2). It is common for the dominant mode to remain coherent for 15–30 sols, with a steady or slowly drifting frequency, until it fades rapidly and is superseded by another mode with a different period and zonal wave number. This pattern of behavior—periods of steady oscillation interrupted by abrupt baroclinic wave transitions—was first identified explicitly by Collins et al. (1996) through analysis and numerical modeling of pressure measurements by VL2. The same phenomenon is apparent in RS measurements of geopotential height (Hinson, 2006; Hinson and Wang, 2010).

The vertical structure of these baroclinic waves depends on the zonal wave number (Banfield et al., 2004; Wang et al., 2005). The longer waves ($s = 1$ and 2) generally have deeper vertical structure than the shorter waves ($s = 3$), but all modes typically produce large temperature oscillations and a substantial meridional heat flux within the lowest scale height of the atmosphere (Hinson, 2006), as expected for a disturbance that arises from baroclinic instability (e.g., Gill, 1982; Barnes, 1984). For example, Fig. 1 shows the observed vertical structure of a wave-2 mode, which achieves

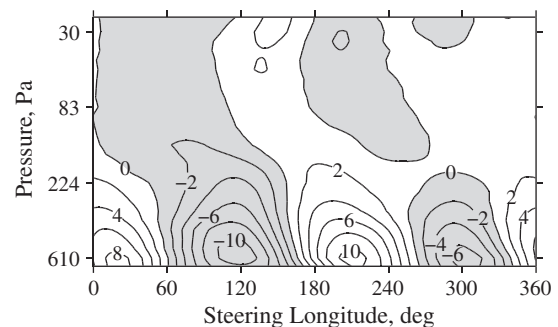


Fig. 1. RS observations of temperature perturbations caused by a baroclinic wave at 69°N during $L_s = 190$ – 200° of MY 26. The “steering longitude” is the zonal coordinate in a reference frame moving eastward at 61°sol^{-1} , the zonal phase speed of the disturbance. The contour interval is 2 K, and shading denotes negative values. The bottom of the figure is ~ 1 km above the surface. The vertical axis is labeled at intervals of one pressure scale height. Adapted from Hinson (2006, Fig. 8).

its peak amplitude in temperature a few kilometers above the ground. In exploring the behavior of these baroclinic waves we will restrict attention to observations near the surface at latitudes of about 50–70°N.

A different type of traveling wave appears in the upper atmosphere of the northern hemisphere between midautumn and midwinter (Wilson et al., 2002; Barnes, 2003; Banfield et al., 2004; Wang, 2007). It is characterized by a small zonal wave number ($s = 1$), a long period (>10 sols), and an amplitude that increases from 1–2 K near the surface to >10 K at the 30-Pa pressure level. Although it plays an important role in the dynamics of the upper atmosphere (Banfield et al., 2004; Wang, 2007), this wave mode has little direct influence on the dynamics near the surface, where the oscillations in temperature and pressure arise primarily from baroclinic waves with shorter periods (<10 sols). We therefore exclude the long-period $s = 1$ traveling wave from further discussion in this paper.

2.2. Viking Lander pressure measurements

We can illustrate several concepts from the preceding discussion through spectral analysis of the VL pressure measurements. VL2 (48°N, 134°E) is at a more favorable location than VL1 (22°N, 312°E) for observing baroclinic waves, which have much larger amplitudes at mid-to-high latitudes than in the tropics (e.g., Barnes, 1981; Banfield et al., 2004; Wang et al., 2005). We therefore focus on data from VL2.

We characterize the time variations in surface pressure p at VL2 by comparing the measurements with a simple model:

$$\hat{p} \equiv \bar{p}(L_s) + p'(t_u), \quad (1)$$

where t_u is universal time on Mars. The first term \bar{p} is the gradual seasonal trend resulting mainly from condensation and sublimation of CO₂, while the second term p' represents the oscillations caused by traveling waves. The wave dynamics are represented using simple periodic basis functions:

$$p'(t_u) \equiv A \cos(2\pi\sigma t_u - \epsilon). \quad (2)$$

The wave model contains three free parameters: the amplitude A , the frequency σ , and the phase ϵ . We define the period $P \equiv \sigma^{-1}$.

When observed from a fixed location on the surface, the frequency σ of a traveling wave can be measured without ambiguity, but the zonal wave number s is elusive (e.g., Barnes, 1980, 1981). We will return to this point in Section 5.

Properties of the traveling waves are determined as follows. We begin by selecting a subset of data spanning 8° of L_s (~ 15 sols). This analysis interval is a compromise between shorter segments, which provide better time resolution, and longer segments, which provide better frequency resolution. Within each subset of data, we solve for the seasonal trend \bar{p} by fitting a quadratic polynomial to samples of p versus L_s . We then search for traveling waves by comparing the wave model with the detrended data $p - \bar{p}$, considering frequencies in the range $0 < \sigma < 2.5 \text{ sol}^{-1}$. For each value of σ , we obtain least squares solutions for A and ϵ that minimize the difference between the wave model and the detrended data.

We applied this method of analysis to all data acquired by VL2; the results from autumn of its second year of operation (MY 13) are shown in Fig. 2. This spectrogram is a composite of solutions for A^2 versus σ from within a sliding 8° window of L_s . There is only one significant interruption in the observations, near $L_s = 229^\circ$. The prominent spectral peaks in Fig. 2 signal the presence of several types of traveling waves (e.g., Barnes, 1981; Zurek and Leovy, 1981; Zurek et al., 1992), including diurnal tides ($\sigma = 1.0 \text{ sol}^{-1}$), semidiurnal tides ($\sigma = 2.0 \text{ sol}^{-1}$), and baroclinic waves ($\sigma < 0.75 \text{ sol}^{-1}$).

The properties of these baroclinic waves have been reported previously (e.g., Barnes, 1981; Ryan and Sharman, 1981; Zurek

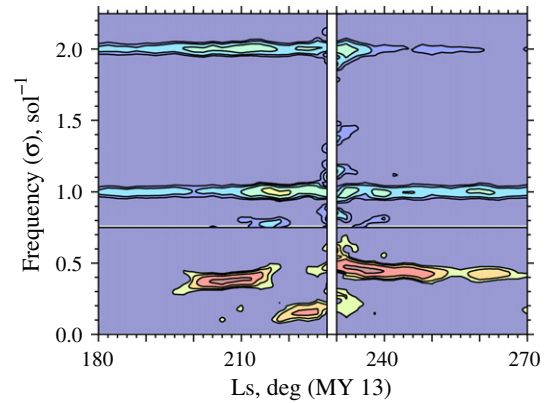


Fig. 2. Spectrogram of variations in surface pressure measured by VL2, showing the evolution of baroclinic waves and thermal tides during autumn of MY 13. Different contour levels are used in the upper and lower portions of the figure. The peak contour corresponds to an amplitude of 1.2% for thermal tides ($\sigma > 0.75 \text{ sol}^{-1}$) and 3.0% for baroclinic waves ($\sigma < 0.75 \text{ sol}^{-1}$). Each successive contour represents a doubling of power. The average surface pressure \bar{p} increased from ~ 770 Pa at $L_s = 180^\circ$ to ~ 980 Pa at $L_s = 270^\circ$.

et al., 1992; Collins et al., 1996), but Fig. 2 is effective at highlighting their key attributes: steady oscillations that persist for a span of 15–30 sols punctuated by abrupt transitions among modes with different frequencies. Three prominent modes appear within this subset of observations: (1) $\sigma = 0.38 \text{ sol}^{-1}$ ($P = 2.6$ sols) at $L_s = 200$ – 216° , (2) $\sigma = 0.15 \text{ sol}^{-1}$ ($P = 6.7$ sols) at $L_s = 218$ – 227° , and (3) $\sigma = 0.45 \text{ sol}^{-1}$ ($P = 2.2$ sols) at $L_s = 230$ – 252° . The first and third modes are the strongest, with peak amplitudes of $\sim 3\%$ (~ 25 Pa).

According to numerical simulations (Collins et al., 1996), the baroclinic wave transitions are induced by dynamical jostling from the thermal tides. Fig. 2 provides circumstantial evidence in support of this conclusion. The amplitude of both the diurnal and semidiurnal tides varies significantly with time, possibly in response to regional dust storms at some remote location (e.g., Leovy and Zurek, 1979; Leovy, 1981; Zurek and Leovy, 1981; Wilson and Hamilton, 1996). In particular, the amplitude of the diurnal tide increases from $\sim 0.6\%$ at $L_s = 200$ – 210° to more than 1.2% at $L_s = 215$ – 220° , with a peak value of $\sim 1.4\%$ near $L_s = 216^\circ$. The baroclinic wave transition at about $L_s = 217^\circ$ may have been triggered by this transient intensification of the diurnal tide.

Things were not as orderly at VL2 during the subsequent winter season, as shown in Fig. 3. The frequency distribution of the baroclinic waves is trimodal, as noted previously (Barnes, 1981; Zurek

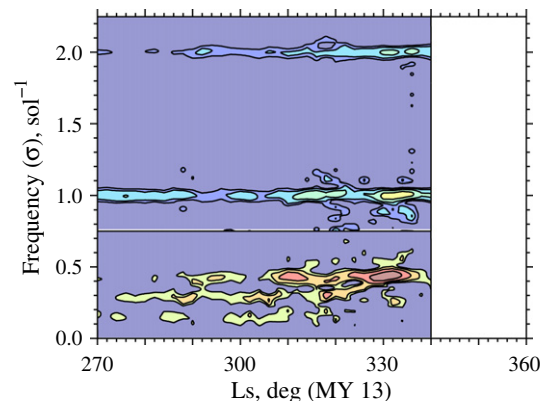


Fig. 3. Spectrogram of variations in surface pressure measured by VL2, showing the evolution of baroclinic waves and thermal tides during winter of MY 13. The format and contour levels are the same as those in Fig. 2. There is a sizable gap in the VL2 data beginning at $L_s = 342^\circ$.

et al., 1992), with notable spectral peaks centered roughly at 0.16 sol^{-1} , 0.29 sol^{-1} , and 0.43 sol^{-1} . Observations by the TES imply that the zonal wave number of the respective modes is probably 1, 2, and 3, so that all three modes have about the same zonal phase speed (Banfield et al., 2004). But the baroclinic wave transitions among modes with different frequencies are less decisive than those in Fig. 2, and the strongest mode at any given time is often accompanied by a secondary mode whose amplitude is comparable to that of the primary. A dominant mode emerged in two intervals, $L_s = 308\text{--}314^\circ$ and $L_s = 324\text{--}336^\circ$, with a period in both cases of 2.3 sols.

The results in Figs. 2 and 3 illustrate fundamental properties of baroclinic waves in the northern hemisphere. In order to develop a more complete description of their behavior, we now turn our attention to data from the atmospheric sounders on MGS.

3. Remote sensing of atmospheric waves

From 1999 to 2006, during the mapping phase of its mission, MGS monitored the structure and dynamics of the martian atmosphere from a nearly circular, Sun synchronous, polar orbit. The TES sounded the atmosphere almost continuously in its nadir viewing mode from $L_s \approx 110^\circ$ of MY 24 through $L_s \approx 80^\circ$ of MY 27, while the RS occultation experiments provided supplementary coverage at selected latitudes and seasons. Atmospheric profiles retrieved from TES and RS observations are highly complementary, and this combination of data yields a more thorough characterization of baroclinic waves than can be obtained from either instrument alone. The advantages of the TES observations include essentially complete global coverage with each latitude sounded twice per orbit (e.g., Smith, 2004; Banfield et al., 2004). The radio occultations provide a unique measure of geopotential height (e.g., Hinson, 2006; Hinson and Wang, 2010) and a roughly 10-fold improvement in vertical resolution (e.g., Hinson et al., 1999; Conrath et al., 2000). The RS observations also continued through northern spring of MY 28, nearly a year after the end of atmospheric sounding by the TES.

In this section we adapt the method of spectral analysis described in Section 2.2 so that it can be applied to TES and RS data. A least squares approach is well suited to the observations considered here, where some samples are missing and the interval between samples is not constant. We use numerical simulations to illustrate the performance of this method of analysis and to characterize the information content of each type of observation.

3.1. Space–time coverage of TES and RS data

We begin by describing the space–time coverage of the TES and RS data, using observations from midwinter of MY 25 as a representative example. (We return to this subset of data in Section 4.) We focus on latitudes of $60\text{--}65^\circ\text{N}$, where both TES and RS observations are available during this interval. We further limit discussion to the 610-Pa pressure level, which is useful for characterizing the behavior of baroclinic waves and their influence on the timing and location of regional dust storms (e.g., Hinson and Wang, 2010).

The TES sounded the atmosphere twice per orbit within this latitude band at local times of 1.6 and 12.8 h. At each local time the longitude steps westward by $\sim 29^\circ$ in the interval of ~ 0.08 sols (~ 118 min) between observations on consecutive orbits. Measurements at the two local times are interleaved but the sample spacing is not uniform. At this latitude the interval between successive overflights alternates between ~ 0.012 sols (~ 18 min) and ~ 0.067 sols (~ 100 min).

During midwinter of MY 25, the RS experiments sounded the atmosphere once per orbit at a latitude of $\sim 63^\circ\text{N}$ and a local time of ~ 8.1 h. Apart from the offset in local time, the RS data have essentially the same space–time sampling as the TES dayside observations.

3.2. Least squares analysis

Atmospheric profiles retrieved from the TES and RS data are distributed in longitude, and Eqs. (1) and (2) must be modified accordingly. Within subsets of data at constant latitude and pressure, we characterize the zonal and temporal variations in temperature T by comparing the measurements with a more general model:

$$\hat{T} \equiv \bar{T}(L_s) + T'(\lambda, t_u). \quad (3)$$

The first term \bar{T} is the seasonal trend, while the second term T' represents the oscillations caused by atmospheric waves, which now depend explicitly on east longitude λ :

$$T'(\lambda, t_u) \equiv A \cos(s\lambda - 2\pi\sigma t_u - \psi). \quad (4)$$

The zonal wave number s now appears as a fourth free parameter in the wave model, in addition to the amplitude A , frequency σ , and phase ψ . We adopt the sign convention that $s \geq 0$. Positive and negative values of σ correspond to eastward and westward traveling waves, respectively, while $\sigma \approx 0$ for quasi-stationary waves.

We use expressions analogous to Eqs. (3) and (4) to model the zonal and temporal variations of geopotential height Z . Note that T is proportional to the vertical derivative of Z for an atmosphere in hydrostatic equilibrium, which is a good approximation in this context. Observations of T and Z therefore provide complementary information about the characteristics of baroclinic waves.

The distribution of the TES and RS observations in longitude and time causes ambiguity in solutions for s and σ . This concept is well understood from the long heritage of atmospheric sounding by satellites in polar orbit (e.g., Chapman et al., 1974; Salby, 1982a,b; Lait and Stanford, 1988; Wu et al., 1995). Nonetheless, we will digress briefly to illustrate the limitations of these observations by applying our method of spectral analysis to synthetic data. These simulations also introduce important details of our methodology.

The synthetic temperature data comprise a superposition of four wave modes sampled over a span of 20 sols at constant latitude (62.5°N) and pressure (610 Pa). One mode is an eastward traveling diurnal wave with $s = 1$, $\sigma = +1 \text{ sol}^{-1}$, and an amplitude of 4.5 K. The other three modes are eastward traveling baroclinic waves, all with the same frequency ($\sigma = +0.4 \text{ sol}^{-1}$), but with different amplitudes and zonal wave numbers (3 K at $s = 1$, 4 K at $s = 2$, and 5 K at $s = 3$). These combinations of s and σ are typical of atmospheric waves observed on Mars (e.g., Wilson et al., 2002; Banfield et al., 2004; Hinson, 2006; Wang, 2007; Hinson and Wang, 2010). The synthetic data sample the atmosphere with the same space–time coverage as the TES data described in Section 3.1.

3.2.1. Observations obtained once per orbit

Consider first the information content of observations obtained once per orbit at a constant local time of 12.8 h. We searched for atmospheric waves by comparing the wave model T' with the synthetic data, considering a range of values for s and σ . For each combination of s and σ , the procedure yields least squares solutions for A and ψ that minimize the difference between the wave model and the synthetic data. Fig. 4 displays the results as a set of periodograms, each showing solutions for A^2 versus σ for a particular value of s .

The periodograms in Fig. 4 contain a narrow spectral peak for each of the four waves in the synthetic data, but false peaks also appear at many other combinations of s and σ . This simulation

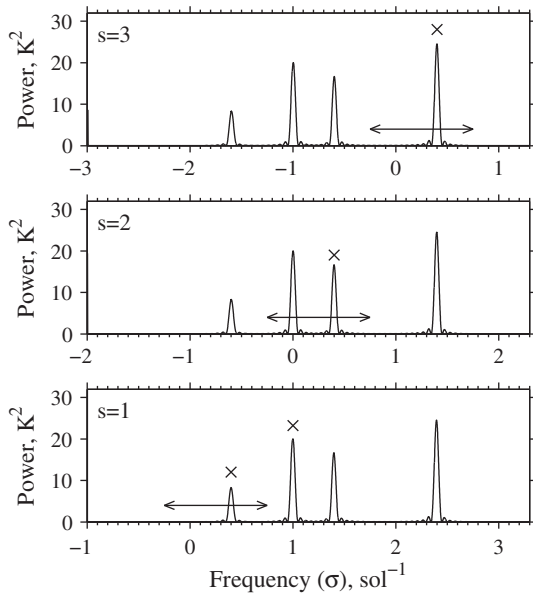


Fig. 4. Results from analysis of synthetic temperature measurements. Observations are obtained once per orbit at a local time of 12.8 h. The periodogram in each panel corresponds to a different assumed value of s . Each wave mode in the synthetic data produces a true spectral peak (marked with an “x”) along with false peaks at other combinations of s and σ that yield the same value of f (see Eq. (5)). The horizontal axis in each panel is shifted so that peaks with the same value of f are vertically aligned.

demonstrates the well known fact that unique solutions for s and σ cannot be derived from observations where the measurement longitude depends systematically on the time of observation (e.g., Conrath, 1981; Lait and Stanford, 1988; Wu et al., 1995). Each wave in the synthetic data can be interpreted in several ways, so that each true spectral peak is accompanied by a set of alternate solutions. For example, the eastward traveling diurnal wave appears at its correct location ($s = 1$, $\sigma = +1 \text{ sol}^{-1}$), but it cannot be distinguished unambiguously from a stationary wave ($s = 2$, $\sigma = 0 \text{ sol}^{-1}$) or a westward traveling diurnal wave ($s = 3$, $\sigma = -1 \text{ sol}^{-1}$). When observed once per orbit at constant local time, the wave corresponding to each combination of s and σ is Doppler shifted by the rotation of Mars to the same apparent frequency:

$$f = \sigma + s/\tau, \quad (5)$$

where τ is the rotation period of Mars. This type of space–time sampling uniquely determines the value of f but only constrains the sum of s and σ . In this case, the limitations of the periodogram can be expressed as follows:

$$\hat{A}^2(s, \sigma) = \hat{A}^2(s + n, \sigma - n/\tau), \quad (6)$$

where \hat{A} is the least squares solution for A , and n is any integer.

There is considerable redundancy among the set of periodograms in Fig. 4. We can capture the information relevant to this investigation by retaining a 1 sol^{-1} range of σ for each value of s . As in previous applications (Hinson, 2006; Hinson and Wang, 2010), we restrict σ to the range

$$-0.25 \text{ sol}^{-1} < \sigma \leq +0.75 \text{ sol}^{-1}, \quad (7)$$

as shown by the horizontal line in each panel of Fig. 4. This choice is guided by previous observations from both VL2 (e.g., Ryan et al., 1978; Barnes, 1980, 1981; Leovy et al., 1985; Zurek et al., 1992) and the TES (Banfield et al., 2004), which show that baroclinic waves on Mars generally travel eastward with periods in the range of 2–10 sols. In our notation, $\sigma > 0$ with a magnitude of $0.1\text{--}0.5 \text{ sol}^{-1}$.

3.2.2. Observations obtained twice per orbit

We conducted a second numerical simulation for the case where observations are obtained twice per orbit at local times of 1.6 and 12.8 h. We changed only the space–time sampling of the synthetic data, which contain the same four wave modes as before. Fig. 5 shows periodograms computed from least squares analysis, analogous to the ones that appear in Fig. 4. The improvement in space–time sampling eliminates many of the false spectral peaks.

There is a simple intuitive explanation for the results in Fig. 5. The observations at each local time provide an independent record of the zonal and temporal variations in temperature. These two subsets of data are concurrent but offset in longitude by $\sim 180^\circ$. This type of space–time sampling reveals unambiguously whether s is odd or even, and the false spectral peaks are now restricted to values of s with the same parity as the correct solution. For example, the periodogram for $s = 2$ is now free of interference from wave modes with $s = 1$ or 3. The ambiguity in observations obtained twice per orbit can be expressed as

$$\hat{A}^2(s, \sigma) = \hat{A}^2(s + 2n, \sigma - 2n/\tau), \quad (8)$$

where n is any integer.

Salby (1982a,b) derived the “Nyquist limits” for observations obtained twice per orbit by a Sun-synchronous satellite, which can be expressed as

$$\left(-1 + \frac{s-1}{4\pi^2}\right) \text{ sol}^{-1} < \sigma < \left(+1 + \frac{s+1}{4\pi^2}\right) \text{ sol}^{-1}, \quad (9)$$

as shown by the horizontal line in each panel of Fig. 5. The width of each frequency window is $\sim 2.05 \text{ sol}^{-1}$, independent of s . This range of σ retains all unique information while eliminating redundancy.

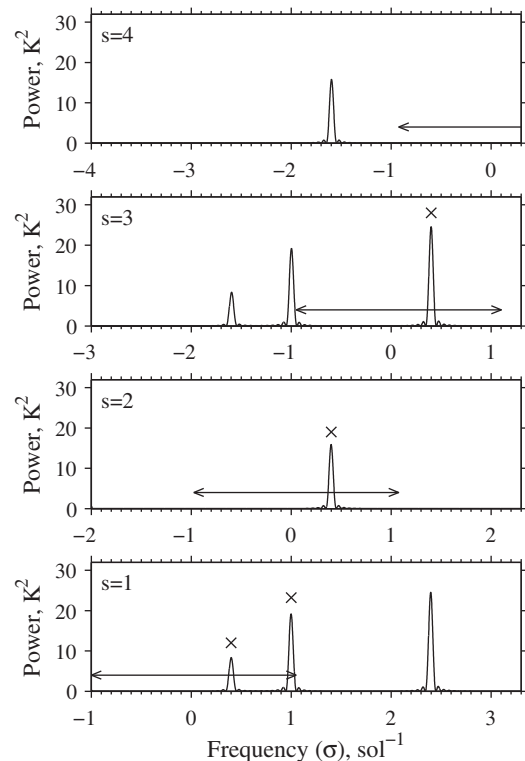


Fig. 5. Results from analysis of synthetic temperature measurements. The only difference between this simulation and the case considered in Fig. 4 is that observations are now obtained twice per orbit at local times of 1.6 and 12.8 h. The increase in the information content of the synthetic data is reflected by a decrease in the number of false spectral peaks. The horizontal lines indicate a set of spectral windows, one for each value of s , that contains all unique information.

Eq. (9) applies for $s = 1$ –4; see Lait and Stanford (1988) for the range appropriate to other values of s .

4. Observations from midwinter of MY 25

In this section we examine MGS data from midwinter of MY 25, deriving a detailed characterization of a weather pattern that affects the timing and location of regional dust storms in the northern hemisphere. We demonstrate that both the atmospheric waves and the dust storms that appear during this interval closely resemble their counterparts from midautumn of MY 27, as reported by Hinson and Wang (2010), confirming the importance of this weather pattern as a basic element of the martian dust cycle.

The discussion within this section is organized as follows. Sections 4.1 and 4.2 characterize the atmospheric dynamics at northern midlatitudes through spectral analysis of both TES and RS observations. Section 4.3 investigates the contemporaneous dust storms observed by the MGS MOC. Section 4.4 summarizes the results and their implications for the martian dust cycle.

This section focuses on a sequence of events that attracted little attention in previous analyses of these data sets by Cantor (2003, MOC), Banfield et al. (2004, TES), Wang et al. (2005, MOC and TES) and Hinson (2006, RS). A careful comparison of the RS and MOC observations, which was absent from previous studies, turns out to be particularly informative.

4.1. Atmospheric waves observed by MGS

We begin with discussion of the TES data, which yield more reliable solutions for s and σ , as explained in Section 3.2. Anomalies in spacecraft operations prevented the TES from collecting data during $L_s = 318.5$ – 325.8° and $L_s = 333.3$ – 340.6° of MY 25, so we restrict attention for now to the intervening period, a span of ~ 13 sols. We further limit discussion to latitudes of 60 – 65°N , where simultaneous RS measurements are available. (This restriction is removed in Section 5.) Each overflight of this latitude band lasted <100 s, sampled a narrow range of longitudes ($<1^\circ$), and yielded ~ 20 TES temperature profiles, but the number varies from orbit to orbit, including a few cases where no data are available. We reduced the noise inherent in the TES retrievals by averaging the results from each cluster of observations.

We characterized the dynamics near the surface by applying the method of analysis described in Section 3.2 to TES measurements of T_{610} , the temperature at 610 Pa. We solved for the seasonal trend \bar{T} by fitting a quadratic polynomial to samples of T_{610} versus L_s . We then searched methodically for atmospheric waves by comparing the wave model T with the detrended data $T_{610} - \bar{T}$, computing a set of periodograms analogous to those in Fig. 5. The results appear in Fig. 6.

Each periodogram in Fig. 6 contains a prominent spectral peak near $\sigma = +0.44 \text{ sol}^{-1}$ ($P = 2.3$ sols). The basis functions T that best fit these spectral features have amplitudes of 5.1 K at $s = 3$, 2.9 K at $s = 2$, and 3.8 K at $s = 1$. This superposition of wave modes is the signature of an eastward traveling baroclinic wave whose amplitude varies strongly with longitude (Banfield et al., 2004; Wang, 2007; Hinson and Wang, 2010); we will return to this topic in Section 4.2. The periodograms in Fig. 6 also contain secondary peaks corresponding to quasi-stationary waves ($\sigma \approx 0 \text{ sol}^{-1}$), with amplitudes of 2.4 K at $s = 1$ and 1.8 K at $s = 2$.

The RS observations suffered fewer interruptions from the spacecraft anomalies mentioned above, and atmospheric sounding continued throughout $L_s = 305.4$ – 334.0° of MY 25. We applied least squares analysis to several subsets of the RS data. For example, Fig. 7a shows periodograms computed from RS measurements of T_{610} during $L_s = 316$ – 330° , a span of ~ 24 sols. (The reason for

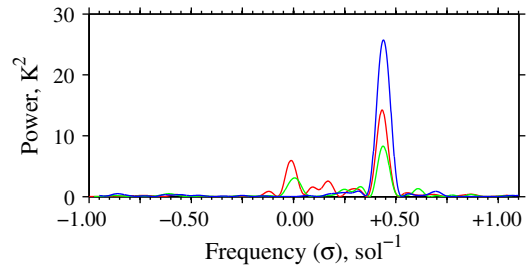


Fig. 6. Periodograms of variations in T_{610} computed from TES nadir measurements at 60 – 65°N during $L_s = 326$ – 333° of MY 25. Observations are obtained twice per orbit at local times of 1.6 and 12.8 h. Results are shown for $s = 1$ (red), $s = 2$ (green), and $s = 3$ (blue). Each periodogram spans the frequency range prescribed in Eq. (9). The spectral peaks near $\sigma = 0.44 \text{ sol}^{-1}$ ($P = 2.3$ sols) correspond to an eastward traveling baroclinic wave. (For interpretation of the references to color in this figure legend, the reader is referred to the web version of this article.)

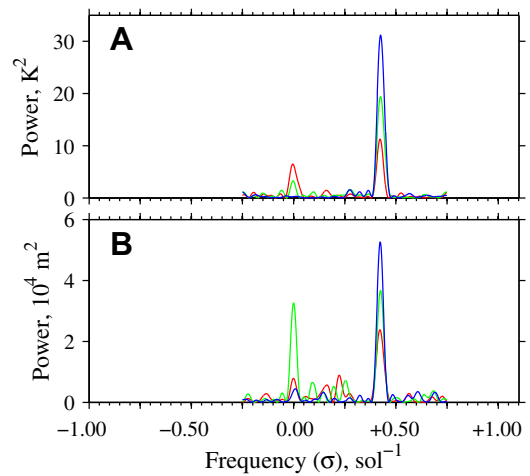


Fig. 7. Periodograms of variations in (A) T_{610} and (B) Z_{610} computed from RS measurements at 63°N during $L_s = 316$ – 330° of MY 25. Observations are obtained once per orbit at a local time of 8.1 h. Results are shown for $s = 1$ (red), $s = 2$ (green), and $s = 3$ (blue). Each periodogram spans the frequency range prescribed in Eq. (7), but the horizontal axis is extended to simplify comparison with Fig. 6. The spectral peaks at $\sigma = 0.43 \text{ sol}^{-1}$ ($P = 2.3$ sols) correspond to an eastward traveling baroclinic wave. (For interpretation of the references to color in this figure legend, the reader is referred to the web version of this article.)

selecting this range of L_s is explained below.) Fig. 7b shows analogous results derived from RS measurements of Z_{610} , the geopotential height at 610 Pa. As in Fig. 6, the variance of these data is concentrated within a few distinct wave modes. Each periodogram in Fig. 7 contains a strong, narrow spectral peak near $\sigma = 0.43 \text{ sol}^{-1}$ ($P = 2.3$ sols). The geopotential field also contains a conspicuous stationary wave ($s = 2$, $\sigma = 0 \text{ sol}^{-1}$) with an amplitude of 180 m.

We surveyed the wave activity in the RS data from midwinter of MY 25 by computing a sequence of periodograms from within a sliding 8° window of L_s (~ 14 sols at this season). Fig. 8 displays the results as a set of spectrograms, which characterize the time evolution of the baroclinic waves and their distribution in s and σ . A strong $s = 2$ mode was present at the start of the interval, with $P = 3.3$ sols ($\sigma = 0.30 \text{ sol}^{-1}$) and a peak amplitude of ~ 4 K at $L_s = 309^\circ$. The $s = 2$ mode subsided at $L_s \approx 315^\circ$, coincident with the intensification of the baroclinic wave depicted in Fig. 7. The second mode had a distinctly shorter period than the first ($P = 2.3$ sols, $\sigma = 0.43 \text{ sol}^{-1}$) and a more complex spectral signature, with a strong peak at $s = 3$ and secondary peaks at $s = 1$ and 2, as shown in Fig. 7. This baroclinic wave produced very regular oscillations of temperature and geopotential during $L_s = 316$ – 330° , but its amplitude had decreased appreciably by the time that observations were

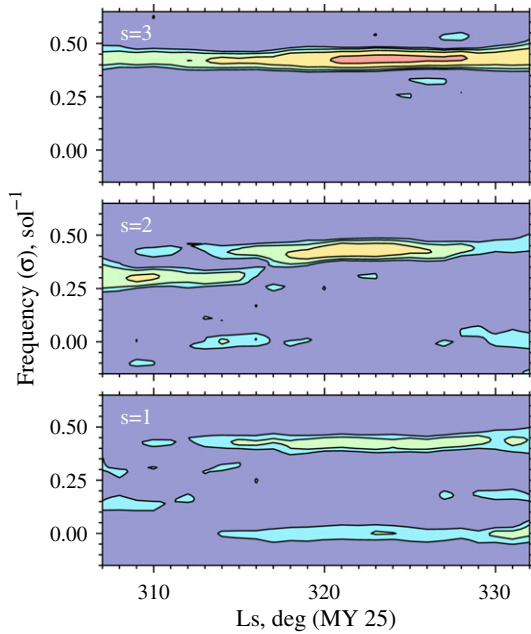


Fig. 8. Spectrograms of space–time variations in RS measurements of T_{610} at 62–65°N, showing the evolution of atmospheric waves during midwinter of MY 25. The figure is a composite of periodograms, like the ones in Fig. 7a, computed from within a sliding 8° window of L_s . Contours are shown at 4, 8, 16, and 32 K^2 .

interrupted by a spacecraft anomaly at $L_s = 334^\circ$. There was little trace of the wave-3 mode when observations resumed at $L_s = 338^\circ$.

The results in Fig. 8 help reconcile the differences between the RS periodograms in Fig. 7a and the TES results in Fig. 6. The RS results are centered on the interval when the baroclinic wave achieved its peak amplitude ($L_s = 316$ – 330°). Owing to data gaps, the TES results cover an interval when the amplitude was fading ($L_s = 326$ – 333°), most noticeably in the spectral component at $s = 2$, while its frequency was increasing gradually.

4.2. The reconstructed waveform

The baroclinic wave that appears during $L_s = 316$ – 330° has a distinctive spectral signature, comprising a set of narrow peaks aligned in frequency ($\sigma = 0.43 \text{ sol}^{-1}$) but with different zonal wave numbers ($s = 1, 2$, and 3). We now look more closely at the nature of this disturbance.

We modeled the temperature field of the atmospheric wave as a superposition of basis functions of the type defined in Eq. (4), one for each significant spectral peak in Fig. 7a. The spectrum is dominated by the three traveling wave modes. We labeled each mode with an index i , obtained least squares solutions for wave parameters (A_i , s_i , σ_i , and ψ_i), and constructed a model for the space–time variations of T_{610} by combining the results:

$$T''(\lambda, t_u) = \sum_{i=1}^3 A_i \cos(s_i \lambda - 2\pi \sigma_i t_u - \psi_i). \quad (10)$$

Fig. 9 shows the space–time structure of the reconstructed waveform T'' . This baroclinic wave travels steadily eastward and its amplitude varies strongly with longitude. The separation in longitude between zero crossings, though not uniform, is $\sim 60^\circ$, consistent with a wave-3 mode. The three basis functions in Eq. (10) add constructively near 240°E , north of Alba Mons, where the magnitude of T'' exceeds 10 K. There is a secondary maximum near 60°E , with a magnitude of ~ 5 K. A deep minimum appears near 120°E in northern Utopia Planitia, near the longitude of VL2.

In subsequent discussion we will refer to the composite waveform in Fig. 9 as the “ $s = 3$ baroclinic wave” or the “wave-3 mode.”

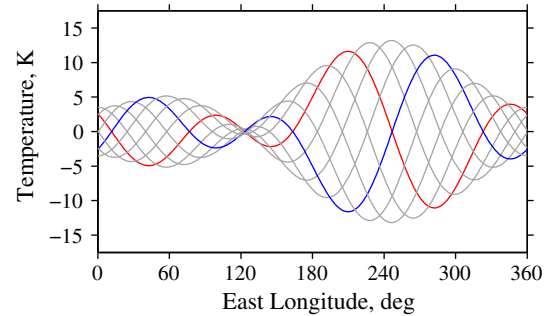


Fig. 9. Variations in T_{610} caused by a baroclinic wave at 63°N during $L_s = 316$ – 330° of MY 25. Each curve shows a snapshot at fixed t_u of the waveform reconstructed from spectral analysis of RS data, as in Eq. (10). The set of curves tracks the eastward motion of the waveform at eight values of t_u , spread evenly across the 2.3-sol period of the wave. Two waveforms are color coded for future reference. (For interpretation of the references to color in this figure legend, the reader is referred to the web version of this article.)

The strong zonal modulation of amplitude is an intrinsic feature of this disturbance (and implicit in its abbreviated name), as we will show in Section 5.

We used the same approach to model the geopotential field of the atmospheric wave. The results appear in Fig. 10. In this case the reconstructed waveform Z'' is a superposition of five basis functions: three traveling waves ($s = 1, 2$, and 3) and two stationary waves ($s = 1$ and 2). The $s = 1$ stationary wave is relatively weak, as shown in Fig. 7b, but we include its contribution for consistency with the results reported by Hinson and Wang (2010). The magnitude of the fluctuations in Z'' varies strongly with longitude, exhibiting the same general pattern of zonal modulation as T'' . Both stationary waves contain a ridge at $\sim 240^\circ\text{E}$, which accounts for the strong asymmetry between the peaks ($+900$ m) and troughs (-300 m) of Z'' at this longitude.

The results in Fig. 10 are at a latitude and pressure level where the wind field of baroclinic eddies and stationary waves should remain near geostrophic balance (Hinson, 2006; Hinson and Wang, 2010). Hence,

$$v'' \approx \frac{g}{f_c r_m \cos \phi} \frac{\partial Z''}{\partial \lambda}, \quad (11)$$

where v'' is the meridional wind speed (positive northward), g is the acceleration of gravity, f_c is the Coriolis parameter, r_m is the radius of Mars, and ϕ is latitude. We characterized the variations of v'' by applying Eq. (11) to each reconstructed waveform of Z'' . The results appear in Fig. 11.

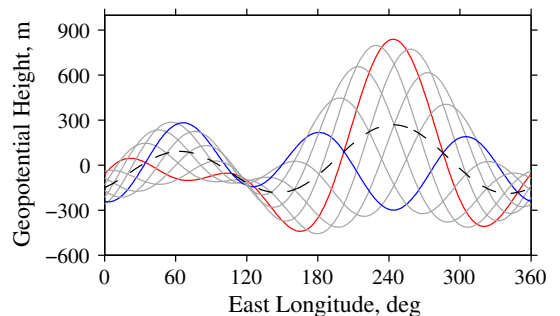


Fig. 10. Variations in Z_{610} caused by a baroclinic wave and two stationary waves at 63°N during $L_s = 316$ – 330° of MY 25, displayed in the same format as Fig. 9. The dashed curve shows the contribution by stationary waves with $s = 1$ and 2. The red and blue curves show results at the same time steps as their counterparts in Fig. 9. (For interpretation of the references to color in this figure legend, the reader is referred to the web version of this article.)

As noted previously, the $s = 3$ baroclinic wave achieves its peak amplitude in Z'' within a roughly 180° band of longitude centered on Alba Mons. The stationary waves also appear to be anchored to this topographic feature, resulting in a meridional wind field with strong zonal modulation and a pronounced north–south asymmetry. The northward winds are strongest ($>20 \text{ m s}^{-1}$) at longitudes of $170\text{--}250^\circ\text{E}$, west of Alba Mons, while the southward winds are strongest ($<-20 \text{ m s}^{-1}$) at longitudes of $240\text{--}320^\circ\text{E}$, east of Alba Mons. This asymmetry is a consequence of the $s = 2$ stationary wave, as shown by the dashed curve in Fig. 11.

The meridional winds implied by these observations vary widely among the major topographic basins of the northern hemisphere. In northern Acidalia Planitia (310°E), the peak southward winds (-25 m s^{-1}) are much stronger than the peak northward winds ($+10 \text{ m s}^{-1}$). The reverse is true in northern Arcadia Planitia (200°E), where the peak northward winds ($+30 \text{ m s}^{-1}$) are about twice as strong as the peak southward winds (-15 m s^{-1}). The winds in northern Utopia Planitia (110°E) are relatively weak with a southward bias, oscillating between -10 and $+1 \text{ m s}^{-1}$.

The $s = 2$ stationary wave is an important component of this weather pattern, as shown in Figs. 7b, 10, and 11, but it exhibits much less variability than the baroclinic waves. Its zonal phase remains essentially constant, independent of L_s (Banfield et al., 2003, Fig. 10), with characteristic zonal variations in geopotential that conform broadly to the surface topography of the northern hemisphere (Hinson, 2006; Hinson and Wang, 2010). This produces a persistent zonal asymmetry in the meridional wind field at mid-to-high northern latitudes throughout autumn and winter, when the amplitude of the $s = 2$ stationary wave is significant.

In the next section we investigate the influence of the $s = 3$ baroclinic wave on the timing and location of dust storms in the topographic basins of the northern hemisphere. Before proceeding, we note one other property of the results in Figs. 9–11. Each waveform of T' lags the concurrent waveform of Z'' by $\sim 90^\circ$ of phase ($\sim 30^\circ$ of longitude), so that T' and v'' are nearly in phase. The resulting poleward heat flux is substantial, with a zonal mean value of $\sim 60 \text{ K m s}^{-1}$ at the 610 Pa pressure level.

4.3. MOC images of dust storms

The MGS MOC included a pair of wide angle (WA) cameras that routinely mapped the surface and atmospheric aerosols in two wavelength bands, one at 575–625 nm (red) and the other at 400–450 nm (blue) (e.g., Malin et al., 1992; Cantor et al., 2001). Image swaths from successive orbits overlap in longitude, so that the WA cameras provide a daily global survey of dust storms and ice

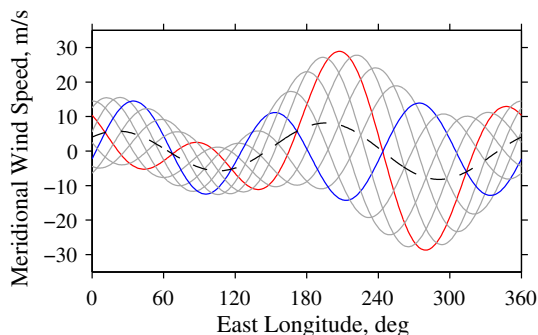


Fig. 11. The meridional winds at 610 Pa implied by geostrophic balance at 63°N during $L_s = 316\text{--}330^\circ$ of MY 25. The set of solid curves was derived by applying Eq. (11) to each reconstructed waveform of Z'' in Fig. 10. Positive winds are northward. The dashed curve shows the contribution from stationary waves. The red and blue curves show results at the same time steps as their counterparts in Figs. 9 and 10. (For interpretation of the references to color in this figure legend, the reader is referred to the web version of this article.)

clouds at a uniform resolution in most cases of 7.5 km per pixel (Cantor et al., 2001; Wang and Ingersoll, 2002; Cantor, 2007).

The MOC observed several notable dust storms in the topographic basins of the northern hemisphere during midwinter of MY 25, as summarized by Wang et al. (2005) and Wang (2007). Arcadia and Utopia were much less active than Acidalia, which experienced several “cross-equatorial” storms that transported dust from high northern latitudes into the southern hemisphere. We will closely examine one of these events, presenting the results in a format that allows direct comparisons with dust storms observed in midautumn of MY 27 (Hinson and Wang, 2010). In characterizing the morphology and evolution of these regional dust storms, we rely on Mars Daily Global Maps (MDGMs), which were assembled from contiguous groups of WA swaths using the procedure described by Wang and Ingersoll (2002).

Fig. 12 shows standard “color” MDGMs constructed from WA images in the red and blue wavelength bands (Wang and Ingersoll, 2002). Fig. 13 shows a “hybrid” version of the same 2-sol sequence, in which the effects of atmospheric dust are enhanced through image processing (Hinson and Wang, 2010). Each hybrid image is derived from a pair of red-filter MDGMs, one that contains a dust storm and another showing the same scene two sols earlier when the atmosphere is relatively clear:

$$I_H = I_D + (I_D - I_R). \quad (12)$$

Here, I_D is the dust storm image, I_R is the “clear” reference image, and I_H is the hybrid. The expression in parentheses accentuates the dust storm, which is generally brighter than an ice-free surface, but its effect is negligible outside the boundaries of the dust storm, where I_D and I_R are essentially the same.

The hybrid image allows the boundaries of the dust storms to be identified with greater confidence. Fig. 13a is also effective in highlighting three local dust storms that appeared within the low-elevation outflow channel of Kasei Valles (300°E , 27°N), where the bright dust clouds contrast sharply with the low surface albedo.

Figs. 12 and 13 depict a distinctive type of regional dust storm that occurs in Acidalia in both midautumn and midwinter of most years (Cantor et al., 2001; Wang et al., 2003, 2005; Cantor, 2007; Wang, 2007; Hinson and Wang, 2010). In its initial “frontal” stage (Fig. 13a), the dust storm is elongated in the zonal direction, extending more than 1500 km from northern Tempe Terra on the west into Acidalia Planitia on the east, with a curving southern boundary. In the subsequent “flushing” stage (Fig. 13b), the storm

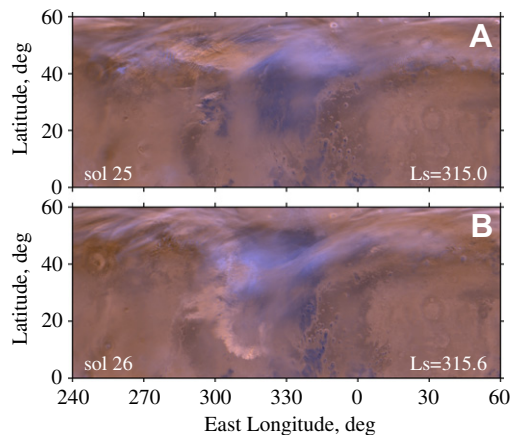


Fig. 12. Color MDGMs from two consecutive sols showing the development of a regional dust storm in Acidalia in midwinter of MY 25. The image in the lower panel appears in a different format in Wang et al. (2005, Fig. 5d). See Fig. 13 for further discussion. The MOC recorded these images on sols 25 and 26 of mapping subphase E12 (http://www.msss.com/moc_gallery/).

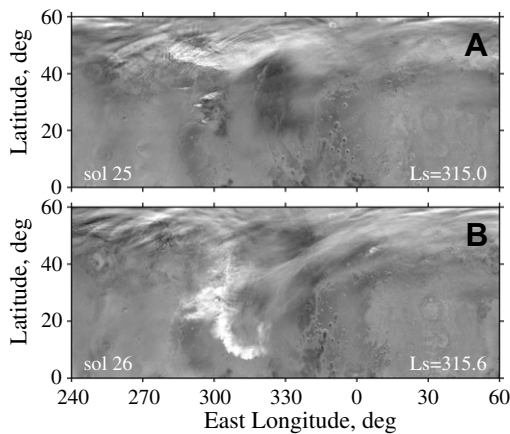


Fig. 13. Alternate view of the dust storm sequence in Fig. 12. Each panel shows a hybrid MDGM in which the effects of atmospheric dust have been enhanced through image processing (see Eq. (12)). (Top) A frontal dust storm appears at 280–330°E, 40–50°N, northeast of Tempe Terra. (Bottom) On the following sol a flushing dust storm sweeps southward along the western boundary of Acidalia and Chryse. This pair of hybrids was constructed using reference images from (top) sol 23 and (bottom) sol 24.

travels rapidly southward through western Acidalia, past Chryse Planitia, and into Xanthe Terra. The apparent motion of the southern boundary of the dust storm, from $\sim 40^\circ\text{N}$ to $\sim 10^\circ\text{N}$ in 1 sol, implies an average southward wind speed of $\sim 20\text{ m s}^{-1}$. During the flushing stage of the storm, dust also spreads westward into the outflow channel of Kasei Valles, obscuring both the surface and any remnants of the local dust storms of the preceding sol. The dust storm sequence in Fig. 13 occurred at $L_s = 315\text{--}316^\circ$, as the $s = 3$ baroclinic wave increased in amplitude to become the dominant mode.

A meridionally extended band of dust appears in Fig. 13b near 305°E , where the topography rises steeply to the west. This may reflect the presence of a western boundary current (WBC)—a shallow, topographically-induced intensification of the meridional winds of the Hadley circulation. The existence of WBCs on Mars is predicted by Mars General Circulation Models (MGCMS) (Joshi et al., 1994, 1995; Wilson and Hamilton, 1996), but no direct measurements of this component of the martian wind field are currently available. According to these numerical simulations, the topography in western Acidalia is highly conducive to the formation of a WBC, with a strong southward flow expected at northern winter solstice.

Wang et al. (2005) and Wang (2007) examined MDGMs from throughout MY 24–26, searching for dust storms that appear to originate from frontal activity in the northern hemisphere. This effort yielded a comprehensive catalog that includes the location, time of occurrence, and other properties of each event. We used the results of this survey to characterize the spatial and temporal distribution of frontal, flushing, and cross-equatorial dust storms during winter of MY 25 ($L_s = 270\text{--}360^\circ$). The MDGMs from this interval include 96 observations of such storms in various stages of their life cycle. In many cases the evolution of a storm can be traced through several successive sols, as in Fig. 13, so that the catalog includes multiple entries for any storm whose duration exceeds 1 sol.

We sorted the catalog by areographic region and computed the cumulative “dust storm count”, defined as the number of events observed between winter solstice and a given value of L_s . This statistic weights each dust storm by its duration in sols, which gives a more accurate indication of its potential impact on the thermal structure and circulation of the atmosphere.

Fig. 14 summarizes the distribution of these dust storms in L_s , latitude, and areographic region. Two patterns are apparent in

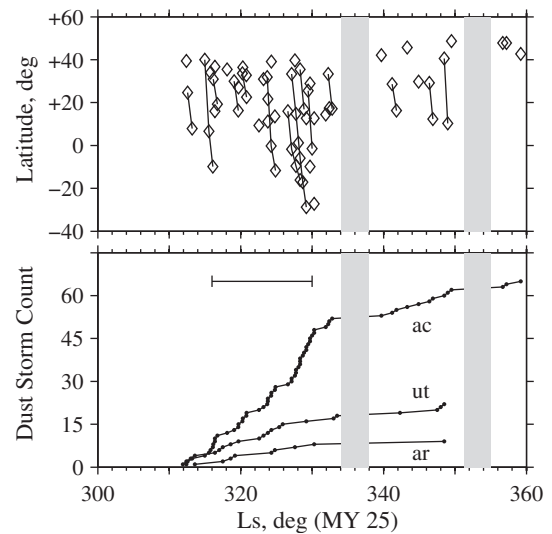


Fig. 14. Distribution of frontal and flushing dust storms during winter of MY 25. The top panel shows the distribution in L_s and latitude of storms that originate in Acidalia. Diamonds mark the time and location of each storm whose morphology and history are indicative of frontal activity and southward motion. Lines connect sequences of activity that can be traced through successive sols. The bottom panel shows a cumulative summation of events originating in Acidalia (ac), Utopia (ut), and Arcadia (ar). No MOC WA images are available in the shaded regions. An intense $s = 3$ baroclinic wave appeared in the interval marked by the horizontal line. Adapted from Wang (2007, Fig. 1).

these observations. First, far more events originated in Acidalia (65) than in Utopia (22) or Arcadia (9). Second, the Acidalia storms are largely confined to the period dominated by the $s = 3$ baroclinic wave ($L_s = 316\text{--}330^\circ$). Dust storms are absent in early winter ($L_s = 270\text{--}312^\circ$) and only a handful occurred after $L_s = 338^\circ$.

Most of the Acidalia dust storms denoted in Fig. 14 were weaker than the event shown in Fig. 13, with one notable exception. A cross-equatorial storm of comparable intensity began 15 sols later at $L_s = 324^\circ$; its structure and evolution are depicted in a 3-sol sequence of MOC WA images by Cantor (2003, Fig. 4). A significant flushing dust storm appeared nearly simultaneously in Utopia (Wang et al., 2005, Fig. 5f). The cumulative effect of these events is significant, resulting in substantial seasonal modulation in the dust loading of the atmosphere, as discussed in Section 5.3.

4.4. The timing and location of regional dust storms

Figs. 6–14 characterize the $s = 3$ baroclinic wave and the concurrent regional dust storms. Wave-3 eddies are relatively compact, which steepens the zonal gradient of geopotential, intensifies the meridional winds, and promotes dust lifting and advection. Owing to the zonal modulation of wave amplitude and the presence of a substantial $s = 2$ stationary wave, the southward winds are considerably stronger in Acidalia than in Arcadia and Utopia. Moreover, the intermittence of the wave-3 mode restricts its influence to a span of ~ 24 sols. The dust storms described in Section 4.3 reflect the basic features of this distinctive weather pattern, which account for both their timing and location.

Another example of this phenomenon was reported previously by Hinson and Wang (2010). MDGMs from autumn of MY 27 tracked more than a dozen regional dust storms in the northern hemisphere, culminating in an intense sequence of flushing storms in Acidalia. The enhancement of dust storm activity within Acidalia coincided with the appearance during $L_s = 220\text{--}228^\circ$ of a wave-3 mode that closely resembles its counterpart from $L_s = 316\text{--}330^\circ$ of MY 25. A comparison of Figs. 10 and 11 with the corresponding results in Hinson and Wang (2010, Figs. 15 and 16) demonstrates

that the dynamics near the surface at midlatitudes were essentially the same during these two intervals. In both cases, the $s = 3$ baroclinic wave strongly influences the timing and location of flushing dust storms in the northern hemisphere.

5. Observations from other seasons and years

In this section we further characterize the behavior of the $s = 3$ baroclinic wave by presenting an assortment of results derived from TES, RS, and VL observations. The discussion emphasizes three points: (1) the basic properties of the wave-3 mode are largely the same whenever it appears, (2) it is the dominant mode in some intervals but remains dormant for extended periods, and (3) this intermittence plays an important role in the annual dust cycle.

In our analysis of the TES and RS data, we restrict attention to the 610-Pa pressure level, focusing on wave activity that contributes directly to dust lifting and dust storm evolution. At this pressure level baroclinic waves generate strong temperature fluctuations at latitudes of about 50–70°N and at seasons between late summer and early spring (e.g., Banfield et al., 2004; Wang et al., 2005, 2007). TES profiles are available at this range of latitudes and seasons in MY 24–26 (Smith, 2004). The RS observations provide complementary coverage in selected seasons of MY 24–26 (Hinson, 2006), and they also extend through MY 27 (Hinson and Wang, 2010), well after the end of atmospheric sounding by the TES.

The latitude coverage of the RS observations ranges from ~60°N to ~75°N at the seasons of interest here, as determined by the MGS orbit geometry and the relative positions of Earth and Mars. The TES provides complete latitude coverage, and we explored the behavior of baroclinic waves by applying spectral analysis to observations from several latitude bands, each 5° wide, with mid-points of 55°N, 57.5°N, 62.5°N, and 67.5°N.

5.1. Zonal modulation of baroclinic waves

The zonal modulation apparent in Figs. 9–11 is an intrinsic feature of the $s = 3$ baroclinic wave. We will illustrate this point by examining subsets of data from autumn of MY 24 and 27. Only the TES was sounding the atmosphere in the first interval, while the second was covered only by RS observations. This comparison also reveals some notable similarities between the weather observed in the two years.

An intense $s = 3$ baroclinic wave appears in midautumn of both MY 24 and 27, achieving its peak amplitude at $L_s = 224^\circ$ in both years. Fig. 15 shows periodograms from the interval in each year when the mode is strongest, $L_s = 220$ – 228° . In both cases the baroclinic wave has the same distinctive spectral signature as the one shown in Fig. 7, comprising three narrow peaks with the same frequency but different zonal wave numbers. There is little difference between the results from MY 24 and 27. For example, the frequency is essentially the same in the two years: $\sigma = 0.48 \text{ sol}^{-1}$ in MY 24 and $\sigma = 0.49 \text{ sol}^{-1}$ in MY 27.

We used Eq. (10) to model the temperature variations associated with this pair of wave-3 modes. The results appear in Fig. 16. The space–time variations of T_{610} from these two years are essentially the same, and they closely resemble the corresponding result from midwinter of MY 25 (Fig. 9). The wave amplitude is largest near 250°E longitude, with a secondary maximum near 70°E and a minimum near 140°E. This pattern persists across a range of latitudes in MY 24, as shown in Fig. 16b and c. At 55°N the zonal modulation of wave amplitude is less pronounced, but the amplitude still varies with longitude by a factor of 3, from a minimum of 5 K to a maximum of 15 K.

The results in Figs. 7, 9, 15 and 16 illustrate two important points. First, the $s = 3$ baroclinic wave exhibits the same pattern

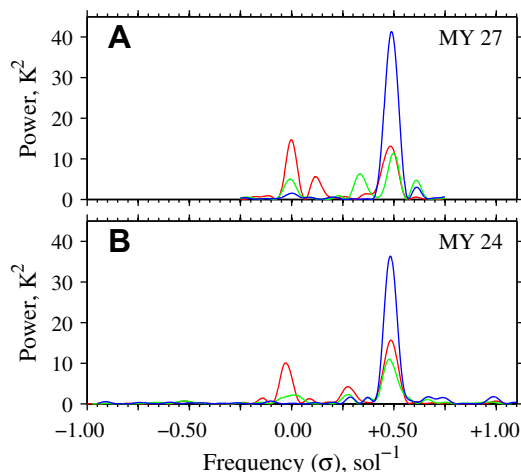


Fig. 15. Periodograms of T_{610} during $L_s = 220$ – 228° of two martian years. These results were derived from (A) RS measurements at 65°N in MY 27, and (B) TES measurements at 60–65°N in MY 24. The color denotes the zonal wave number: $s = 1$ (red), $s = 2$ (green), and $s = 3$ (blue). The superposition of spectral peaks near (A) $\sigma = 0.49 \text{ sol}^{-1}$ and (B) $\sigma = 0.48 \text{ sol}^{-1}$ is the signature of an eastward-traveling $s = 3$ baroclinic wave. (For interpretation of the references to color in this figure legend, the reader is referred to the web version of this article.)

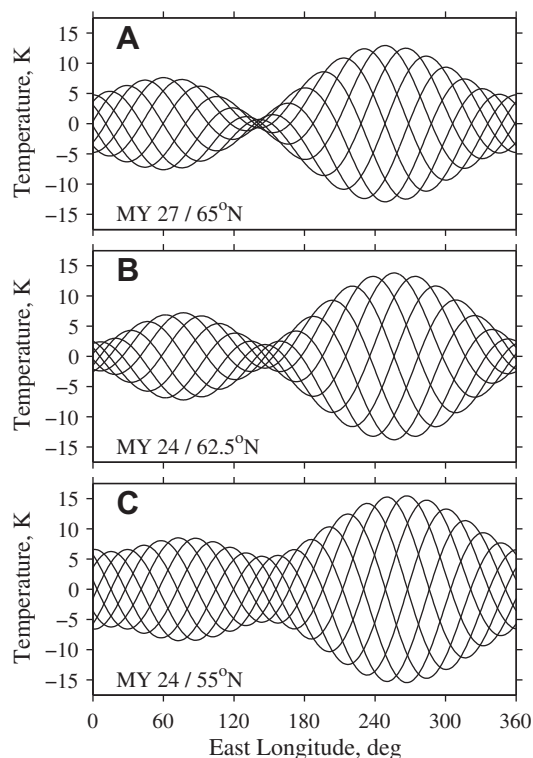


Fig. 16. Reconstructed waveforms of T_{610} , showing the zonal structure and time variations of the $s = 3$ baroclinic wave during $L_s = 220$ – 228° of two martian years: (A) MY 27 at 65°N, (B) MY 24 at 62.5°, and (C) MY 24 at 55°N. The periodograms corresponding to (A) and (B) appear in Fig. 15. See the caption to Fig. 9 for further discussion.

of strong zonal modulation whenever it appears. Our analysis of TES and RS observations from other seasons and years supports this conclusion. Second, the basic properties of a baroclinic wave, such as s and P , and the time interval in which it appears sometimes repeat closely in different years. We will return to this point in Section 6.

Not all baroclinic waves exhibit zonal modulation of wave amplitude. Fig. 17 illustrates this point with periodograms from three intervals, each dominated by a baroclinic wave with a different value of s . For the $s = 1$ baroclinic wave in Fig. 17a, there is no sign of a secondary peak at the same frequency as the primary peak, indicating the absence of appreciable zonal modulation in wave amplitude. In this case the wave can be represented accurately by a single basis function of the form given in Eq. (4). For the $s = 2$ baroclinic wave in Fig. 17b, there is a weak but discernible spectral peak ($s = 3$) at the same frequency as the primary peak, but the resulting zonal modulation of wave amplitude is relatively weak, owing to the disparity in power between the two spectral components. Only the wave-3 mode in Fig. 17c exhibits significant zonal modulation, and there is a close resemblance between its spectral signature and those of its counterparts in Figs. 7 and 15.

Quasi-stationary waves ($\sigma \approx 0 \text{ sol}^{-1}$) appear in all three panels of Fig. 17, with a particularly strong $s = 2$ mode in Fig. 17c. Secondary traveling wave modes also appear in Fig. 17a ($s = 2$, $\sigma = 0.32 \text{ sol}^{-1}$) and Fig. 17c ($s = 1$, $\sigma = 0.15 \text{ sol}^{-1}$), reminiscent of the behavior observed by VL2 in winter of MY 13 (Fig. 3).

The maxima and minima in the amplitude of the wave-3 mode are attached to specific longitudes, as shown in Figs. 9 and 16, which points to surface topography as the source of the modulation. The process that produces this modulation operates most effectively on compact eddies ($s = 3$), where the diameter of a ridge or trough of pressure ($\sim 60^\circ$ of longitude) is comparable to the characteristic zonal scale of prominent topographic features of the northern hemisphere, such as Acidalia, Arcadia, and Utopia.

Zonal variations in the amplitude of baroclinic waves were identified previously through analysis of TES temperature measurements by Barnes (2003, Fig. 1), Banfield et al. (2004, Fig. 20), Wang et al. (2005, Figs. 10 and 11) and Lewis et al. (2007, Fig. 7).

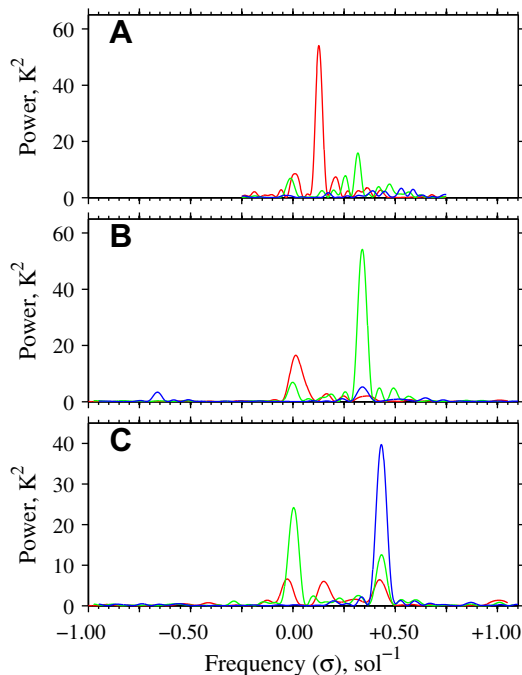


Fig. 17. Periodograms of variations in T_{610} from selected intervals, as derived from (A) RS measurements at 66°N during $L_s = 200\text{--}215^\circ$ of MY 27, (B) TES measurements at $60\text{--}65^\circ\text{N}$ during $L_s = 190\text{--}200^\circ$ of MY 26, and (C) TES measurements at $55\text{--}60^\circ\text{N}$ during $L_s = 306\text{--}318^\circ$ of MY 26. The color denotes the zonal wave number: $s = 1$ (red), $s = 2$ (green), and $s = 3$ (blue). The strongest spectral peak in each panel corresponds to an eastward traveling baroclinic wave with (A) $s = 1$, $\sigma = 0.13 \text{ sol}^{-1}$, (B) $s = 2$, $\sigma = 0.34 \text{ sol}^{-1}$, and (C) $s = 3$, $\sigma = 0.43 \text{ sol}^{-1}$. (For interpretation of the references to color in this figure legend, the reader is referred to the web version of this article.)

However, these investigations used a relatively long analysis interval (30° of L_s), and the boundaries of the intervals are not aligned with baroclinic wave transitions, so that each interval often contains several modes with different values of s and P . The results are therefore difficult to interpret, owing to the dependence of the amplitude modulation on the value of s .

5.2. A multi-year survey of the wave-3 mode

We applied spectral analysis to a broad range of TES and RS observations, solving for basic properties of traveling waves at the 610-Pa pressure level and monitoring their seasonal evolution during MY 24–27. This survey allowed us to identify intervals when the $s = 3$ baroclinic wave satisfies two criteria: (1) it is the strongest mode near the surface, and (2) it persists for at least 10 sols. Table 1 summarizes the results.

Many of the entries in Table 1 have been identified previously (Banfield et al., 2004; Wang et al., 2005; Hinson, 2006; Wang, 2007; Hinson and Wang, 2010), but this is the first uniform survey of the complete set of observations. The wave-3 mode appears within two seasonal windows, one in midautumn at $L_s \approx 220\text{--}250^\circ$ and another in midwinter at $L_s \approx 305\text{--}340^\circ$. The most common value for the period is 2.3 sols, but it decreases notably during midautumn of both MY 24 and 27 (intervals a2 and a4). These intervals are unique in that the period of the wave-3 mode—slightly greater than 2.0 sols—is closer to commensurability with the diurnal thermal tide than at any other season, a possible consequence of nonlinear coupling between these two types of atmospheric waves.

Table 1 also lists several entries derived through spectral analysis of surface pressures measured by VL1 and VL2, as discussed in Section 2.2. The zonal wave number is not known with certainty, but we have inferred that $s = 3$ for the cases listed in Table 1 because of their similarity in both frequency and time of occurrence to wave-3 modes that appear in MY 24–27. The boundaries of interval w3 are not well determined, owing to sporadic gaps in the VL1 pressure measurements.

The wave-3 mode dominates the dynamics near the surface at mid-to-high northern latitudes in intervals a2, w4, w5, and w6, as confirmed through spectral analysis of TES observations at $50\text{--}70^\circ\text{N}$. The mode is also quite prominent at the latitude where RS and VL observations are available in intervals a1, a4, a5, w1, w2, and w3. On the other hand, the wave-3 mode that appears in

Table 1

The estimates for σ and P were derived through spectral analysis of VL measurements of surface pressure, TES measurements of T_{610} , and RS measurements of T_{610} and Z_{610} . Both TES and RS are listed in column 6 when simultaneous observations are available, with the primary source listed first.

| Observations of the $s = 3$ baroclinic wave | | | | | |
|---|-----------|--------------------|--------------------------------|------------|------------|
| Label | Mars year | L_s ($^\circ$) | σ (sol^{-1}) | P (sols) | Instrument |
| <i>Autumn</i> | | | | | |
| a1 | 13 | 230–252 | 0.45 | 2.2 | VL2 |
| a2 | 24 | 219–230 | 0.48 | 2.1 | TES |
| ... | 25 | ... | ... | ... | TES |
| a3 | 26 | 228–242 | 0.46 | 2.2 | TES, RS |
| a4 | 27 | 220–228 | 0.49 | 2.0 | RS |
| a5 | 27 | 230–238 | 0.43 | 2.3 | RS |
| <i>Winter</i> | | | | | |
| w1 | 13 | 308–314 | 0.43 | 2.3 | VL2 |
| w2 | 13 | 324–336 | 0.44 | 2.3 | VL2 |
| w3 | 14 | 308–326 | 0.43 | 2.3 | VL1 |
| w4 | 24 | 316–339 | 0.44 | 2.3 | TES, RS |
| w5 | 25 | 316–330 | 0.43 | 2.3 | RS, TES |
| w6 | 26 | 306–318 | 0.43 | 2.3 | TES |
| w7 | 27 | 305–312 | 0.44 | 2.3 | RS |
| w8 | 27 | 320–330 | 0.41 | 2.4 | RS |

interval a3 of MY 26 is relatively weak when compared with its counterparts from autumn of MY 13, 24, and 27.

During the growth and decay of the wave-3 mode, the power typically changes by a factor of 2 in $<4^\circ$ of L_s , so that the intervals in Table 1 are generally well defined. For example, Fig. 18 shows the transitions that occur at the boundaries of intervals a2 and w4 in MY 24. A strong wave-3 mode appears within restricted intervals, but its power is greatly reduced in the intervening periods, and this intermittence significantly changes the dynamics near the surface at mid-to-high northern latitudes.

The $s = 3$ baroclinic wave was absent in autumn of MY 25, when Mars experienced a major, planet-enshrouding dust storm, which largely obscured the surface in visible images (e.g. Strausberg et al., 2005; Cantor, 2007) and induced major global changes in the thermal structure and circulation of the atmosphere (e.g., Smith et al., 2002). Similarly, our analysis of data from VL2 implies that the wave-3 mode was weak or absent throughout autumn and winter of MY 12, when Mars experienced two planet-enshrouding dust storms (e.g., Zurek et al., 1992).

There are several intervals in Table 1 when two instruments were sounding the atmosphere simultaneously at mid-to-high northern latitudes, including winter of MY 25 as discussed in Section 4.1. Spectral analysis of the TES and RS observations yields mutually consistent results in these cases. The least reliable results in Table 1 are those from winter of MY 27, owing to a significant offset between the latitude of the RS profiles, which drifted from 78°N at $L_s = 305^\circ$ to 68°N at $L_s = 330^\circ$, and the latitude of maximum eddy amplitude, $\sim 55^\circ\text{N}$ at this season (Banfield et al., 2004; Wang et al., 2005, 2007).

In constructing Table 1 we had intended to include a column listing the peak amplitude associated with each appearance of the $s = 3$ baroclinic wave. This turned out to be more difficult than expected for several reasons: basic differences in the quantities measured by VL2 and the atmospheric sounders, the restricted latitude coverage of both the VL data and the RS profiles, and uncertainty about the effect of vertical resolution on the accuracy of the results from the TES. (Although the TES is clearly quite sensitive to the presence of shallow baroclinic waves, it cannot resolve their vertical structure, which may adversely affect the measurements of wave amplitude.) For these reasons Table 1 contains no estimates of wave amplitude, but representative values can be found in Figs. 9, 10, 11 and 16.

5.3. The influence of the wave-3 mode on the annual dust cycle

Sections 5.1 and 5.2 described the characteristic features of the wave-3 mode, and we now consider its influence on the annual dust cycle.

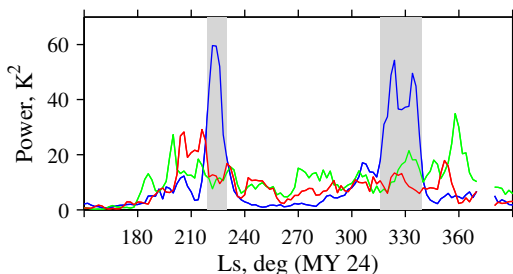


Fig. 18. A survey of baroclinic wave activity in MY 24 at latitudes of $50\text{--}65^\circ\text{N}$, as derived from TES observations of T_{610} . The three curves track the power of the strongest mode at zonal wave numbers of $s = 1$ (red), $s = 2$ (green), and $s = 3$ (blue). The predominant disturbance in both autumn and winter is a wave-3 mode, as highlighted by shading within intervals a2 and w4 of Table 1. See Banfield et al. (2004) and Wang et al. (2005) for discussion of the vertical and meridional structure of these baroclinic waves. (For interpretation of the references to color in this figure legend, the reader is referred to the web version of this article.)

Flushing dust storms occur more frequently in Acidalia than in Utopia or Arcadia, and their distribution in time is skewed by the intermittence of the wave-3 mode, which appears to initiate many of these events. These conclusions have emerged from a series of investigations that identified these patterns of behavior in MGS observations from both autumn and winter of MY 24 (Wang et al., 2003, 2005), winter of MY 26 (Wang, 2007), and autumn of MY 27 (Hinson and Wang, 2010). The results in Section 4 demonstrate that the same conclusions apply to winter of MY 25. More generally, we note that numerous flushing and cross-equatorial dust storms have been observed in Acidalia by the MGS MOC during most of the intervals listed in Table 1, when the dynamics near the surface at mid-to-high northern latitudes are regulated by the wave-3 mode. For example, images of Acidalia dust storms from interval a2 are shown by Cantor et al. (2001, Fig. 11) and Wang et al. (2003, Fig. 1), from interval a3 by Wang et al. (2005, Fig. 5i), from interval a4 by Hinson and Wang (2010, Figs. 5–8), from interval w4 by Wang et al. (2005, Fig. 5b), from interval w5 by Wang et al. (2005, Fig. 5d and 5e) and Cantor (2003, Fig. 4), and from interval w6 by Wang (2007, Fig. 3) and Cantor (2007, Fig. 20).

In Section 4 we identified several factors that contribute to the effectiveness of the wave-3 mode at launching flushing dust storms in Acidalia. First, the compact size of the eddies results in steeper zonal gradients of geopotential and stronger meridional winds than those associated with wave-1 and wave-2 modes. Second, these winds are most intense in the general vicinity of Alba Mons, owing to the zonal modulation in the amplitude of the wave-3 mode. Finally, the presence of a stationary pressure ridge at the longitude of Alba Mons creates a significant southward bias to the meridional winds in Acidalia, which is reinforced by a strong, shallow WBC in western Acidalia. In situ observations in the tropics south of Acidalia attest to the potency of this weather pattern. In operations spanning more than 3 MY, VL1 experienced its strongest near-surface winds during interval w3 (Leovy et al., 1985), with the wave-3 mode making a major contribution.

There is another reason why the wave-3 mode is conducive to flushing dust storms. According to MGCM simulations, a frontal dust storm is most likely to evolve into a flushing storm during daytime, when its southward motion is reinforced by the diurnally varying, near surface winds associated with thermal tides and topographic circulations (Wang et al., 2003; Wilson et al., 2006). This enables the wave-3 mode to promote flushing dust storms by way of its relatively short period, which provides more frequent opportunities for constructive interference between the “frontal” and “tidal” components of the wind field.

A flushing dust storm that crosses the equator can become entrained into the Hadley circulation, resulting in rapid and efficient transport of dust in altitude, longitude, and latitude (e.g., Cantor et al., 2001; Wang et al., 2003; Liu et al., 2003; Wang, 2007). In this way a sequence of cross-equatorial dust storms can trigger a significant change in the global state of the atmosphere, manifested by the sudden appearance of a planet-encircling haze, an intensification of the Hadley circulation, and distinctive global changes in thermal structure. This phenomenon has been observed during midautumn and midwinter of many martian years (e.g., Cantor et al., 2001; Wang et al., 2003; Liu et al., 2003; Smith, 2004, 2009; Cantor, 2007; Wang, 2007; Hinson and Wang, 2010). The signature of the $s = 3$ baroclinic wave is apparent in two characteristics of these events: most begin within the intervals listed in Table 1 and most originate from flushing dust storms in Acidalia. The atmosphere of Mars repeatedly exhibits this pattern of behavior, most notably in interval a2 (Wang et al., 2003; Liu et al., 2003), interval a4 (Hinson and Wang, 2010), and interval w6 (Wang, 2007).

Fig. 19 illustrates important aspects of this chain of events. The TES observed two significant enhancements of dust opacity during MY 24, one in midautumn and another in midwinter. The increase

in opacity at the start of each episode coincides with a rapid intensification of the wave-3 mode after a prolonged absence, as shown in Fig. 19a, and with an increase in the frequency and intensity of flushing dust storms in Acidalia (Wang et al., 2003, 2005; Wang, 2007). Both the intermittence of the wave-3 mode and its capacity to launch sequences of flushing dust storms in Acidalia clearly play an important role in shaping the annual dust cycle.

Observations from other years reinforce this conclusion. In both MY 25 and 26, the characteristic midwinter increase in dust opacity coincides with the emergence of a strong wave-3 mode, as shown in Fig. 19b and c. This pair of wave-3 modes instigated multiple flushing dust storms in Acidalia in MY 25 (Section 4) and MY 26 (Wang, 2007), which contributed significantly to the midwinter increase in dust opacity observed by the TES. Similar behavior occurred in autumn of MY 27, when a prominent wave-3 mode (interval a4) launched a series of flushing dust storms through Acidalia at $L_s = 220\text{--}226^\circ$ (Hinson and Wang, 2010), which culminated in a planet-encircling haze that reached peak opacity at about $L_s = 230^\circ$ (Smith, 2009).

Fig. 19 demonstrates that the most consequential flushing dust storms usually arise from the wave-3 mode. Nevertheless, other baroclinic waves can have a significant impact on the annual dust cycle. For example, a series of vigorous flushing dust storms swept southward through Utopia beginning at about $L_s = 206^\circ$ of MY 26 (Wang, 2007). This sequence of storms triggered the development of a planet-encircling haze that peaked at about $L_s = 215^\circ$, as shown in Fig. 19c. The strongest baroclinic wave at the time of these events had a zonal wave number $s = 2$ (Wang, 2007). Several flushing dust storms occurred subsequently in Acidalia during $L_s = 230\text{--}240^\circ$ (Wang, 2007), when the wave-3 mode had increased in strength (interval a3).

This pattern of seasonal variations in dust opacity was interrupted by a major, planet-enshrouding dust storm in autumn of

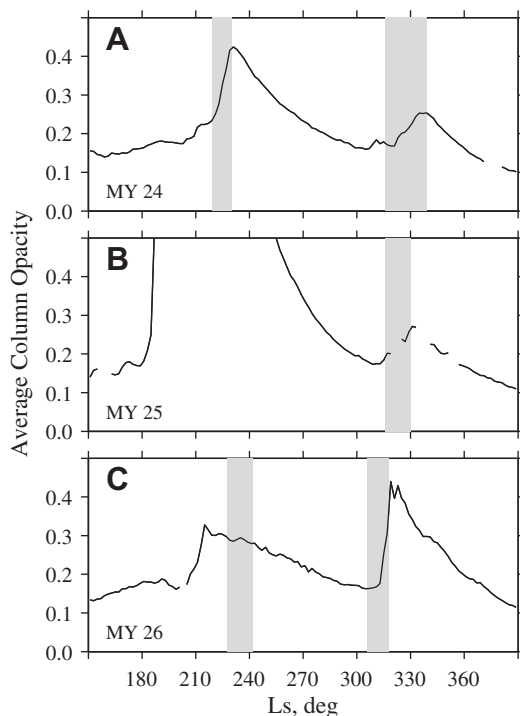


Fig. 19. Comparison of wave activity with seasonal variations in dust opacity during MY 24–26. Shading denotes intervals occupied by a strong $s = 3$ baroclinic wave: (A) a2 and w4 in MY 24, (B) w5 in MY 25, and (C) a3 and w6 in MY 26. The line shows the average column opacity of dust within the tropics, as observed by the TES (Smith, 2004), with a time resolution of 2° in L_s . A similar pattern of seasonal variations in dust opacity recurs in all years without a major, planet-enshrouding dust storm (e.g., Smith, 2004, 2009; Wilson et al., 2006; Lewis et al., 2007).

MY 25 (e.g. Strausberg et al., 2005; Cantor, 2007), as shown in Fig. 19b. Neither the wave-3 mode nor the flushing dust storms of the northern hemisphere contributed appreciably to its origin and evolution.

6. Discussion

We have derived new results concerning the dynamics near the surface in the northern hemisphere of Mars by applying a uniform method of spectral analysis to several different types of atmospheric observations. This method of analysis works equally well for VL measurements of surface pressure (MY 12–14), TES nadir temperature measurements (MY 24–26), and RS measurements of both temperature and geopotential height (MY 24–27). By enabling detailed comparisons among disparate observations, this survey consolidates and extends the results obtained in previous investigations, allowing several basic patterns of behavior to be identified clearly.

There is a distinctive weather pattern associated with the $s = 3$ baroclinic wave, and its regular recurrence in autumn and winter of many martian years plays an important role in the annual dust cycle. Regional flushing dust storms appear more frequently in Acidalia than in Arcadia or Utopia, and their distribution in time is not uniform. Much of this irregularity arises from the detailed properties and intermittence of the wave-3 mode.

More generally, our approach to data analysis may also be useful for identifying similarities and differences among the weather patterns observed at mid-to-high northern latitudes in different martian years. We plan to pursue this topic as part of future research, building on the results in Figs. 15 and 16, which show one instance where nearly identical wave modes appeared in the same seasonal window of different martian years. We will attempt to distinguish patterns of wave activity that repeat from year to year from the chaotic variability that is inherent to some degree in baroclinic waves.

This paper has focused on what can be learned directly from spacecraft observations, but the behavior of baroclinic waves on Mars has also been investigated through numerical simulations with MGCMs (e.g., Barnes et al., 1993; Collins et al., 1996; Hollingsworth et al., 1996, 1997; Hinson and Wilson, 2002; Wilson et al., 2002; Wang et al., 2003; Wilson et al., 2006; Basu et al., 2006; Hollingsworth and Kahre, 2010) as well as through data assimilation (Lewis et al., 2007, 2008). As an illustration of their value in the context of this investigation, we note that MGCMs have provided unique insight in two key areas: the characteristics of WBCs (Joshi et al., 1994, 1995; Wilson and Hamilton, 1996) and the interference between the “frontal” and “tidal” components of the wind field near the surface (Wang et al., 2003; Wilson et al., 2006). Both phenomena probably play an important role in the evolution of flushing dust storms (e.g. Newman et al., 2002; Basu et al., 2006), as discussed in Sections 4.3 and 5.3.

The results reported here provide new constraints for testing the performance of the MGCMs. Two basic questions deserve further attention. Do the models exhibit baroclinic wave transitions? Can they replicate the basic properties of the wave-3 mode, such as its intermittence and the zonal modulation of its amplitude? Attempts to address these questions can lead to improved simulations of flushing dust storms and the annual dust cycle of Mars. After further validation, the MGCMs can yield insight that extends far beyond the limits of direct observations.

Basu et al. (2006) and Wilson et al. (2006) have used the MGCM of the Geophysical Fluid Dynamics Laboratory (GFDL) to simulate the behavior of baroclinic waves, and our findings confirm the accuracy of some aspects of their results. In the northern hemisphere, the simulated wave-3 mode is most active in midautumn

and midwinter, with a lull near winter solstice, in agreement with the results reported here. The period of the simulated wave-3 mode, ~ 2 sols, is also consistent with the observations. However, the wave-3 mode tends to be more persistent and less intermittent in the simulations than in the observations.

The GFDL MGCM also predicts that the amplitude of the wave-3 mode varies strongly with longitude near the surface (Basu et al., 2006; Wilson et al., 2006), confirming the results derived from pre-MGS simulations with the NASA Ames MGCM (Hollingsworth et al., 1996, 1997). Similar behavior has been identified through data assimilation (Lewis et al., 2007). These simulations suggest that the path of shallow, eastward-traveling eddies dips southward into the major topographic basins (Utopia, Arcadia, and Acidalia) but deflects northward around topographic highlands such as Alba Mons. This could account at least in part for the observed zonal modulation in wave amplitude at fixed latitude, as shown in Figs. 9, 10, 11 and 16. More detailed comparisons between the observations and simulations are required to explore this hypothesis.

Acknowledgment

Funding for this research was provided by NASA under Grant NNX08AL24G (Hinson) of the Mars Data Analysis Program.

References

- Banfield, D., Conrath, B.J., Smith, M.D., Christensen, P.R., Wilson, R.J., 2003. Forced waves in the martian atmosphere from MGS TES nadir data. *Icarus* 161, 319–345.
- Banfield, D., Conrath, B.J., Gierasch, P.J., Wilson, R.J., Smith, M.D., 2004. Traveling waves in the martian atmosphere from MGS TES nadir data. *Icarus* 170, 365–403.
- Barnes, J.R., 1980. Time spectral analysis of midlatitude disturbances in the martian atmosphere. *J. Atmos. Sci.* 37, 2002–2015.
- Barnes, J.R., 1981. Midlatitude disturbances in the martian atmosphere – A second Mars year. *J. Atmos. Sci.* 38, 225–234.
- Barnes, J.R., 1984. Linear baroclinic instability in the martian atmosphere. *J. Atmos. Sci.* 41, 1536–1550.
- Barnes, J.R. et al., 1993. Mars atmospheric dynamics as simulated by the NASA AMES general circulation model. II – Transient baroclinic eddies. *J. Geophys. Res.* 98, 3125–3148.
- Barnes, J.R., 2003. Mars weather systems and maps: FFSM analyses of MGS TES temperature data. In: Albee, A.L., Kieffer, H.H. (Eds.), Sixth International Conference on Mars. p. 3127.
- Basu, S., Wilson, J., Richardson, M., Ingersoll, A., 2006. Simulation of spontaneous and variable global dust storms with the GFDL Mars GCM. *J. Geophys. Res. (Planets)* 111, E09004.
- Cantor, B.A., 2003. MGS-MOC observations of martian dust storm activity. In: Albee, A.L., Kieffer, H.H. (Eds.), Sixth International Conference on Mars. p. 3166.
- Cantor, B.A., 2007. MOC observations of the 2001 Mars planet-encircling dust storm. *Icarus* 186, 60–96.
- Cantor, B.A., James, P.B., Caplinger, M., Wolff, M.J., 2001. Martian dust storms: 1999 Mars Orbiter Camera observations. *J. Geophys. Res. (Planets)* 106 (E10), 23653–23688.
- Chapman, W.A., Cross, M.J., Flower, D.A., Peckham, G.E., Smith, S.D., 1974. A spectral analysis of global atmospheric temperature fields observed by the selective chopper radiometer on the Nimbus 4 satellite during the year 1970–1971. *R. Soc. Lond. Proc. Ser. A* 338, 57–76.
- Clancy, R.T. et al., 2000. An intercomparison of ground-based millimeter, MGS TES, and Viking atmospheric temperature measurements: Seasonal and interannual variability of temperatures and dust loading in the global Mars atmosphere. *J. Geophys. Res. (Planets)* 105 (E4), 9553–9572.
- Collins, M., Lewis, S.R., Read, P.L., Hourdin, F., 1996. Baroclinic wave transitions in the martian atmosphere. *Icarus* 120, 344–357.
- Conrath, B.J., 1981. Planetary-scale wave structure in the martian atmosphere. *Icarus* 48, 246–255.
- Conrath, B.J. et al., 2000. Mars Global Surveyor Thermal Emission Spectrometer (TES) observations: Atmospheric temperatures during aerobraking and science phasing. *J. Geophys. Res. (Planets)* 105, 9509–9519.
- Gill, A.E., 1982. *Atmosphere-Ocean Dynamics*. Academic Press, San Diego.
- Hinson, D.P., 2006. Radio occultation measurements of transient eddies in the northern hemisphere of Mars. *J. Geophys. Res. (Planets)* 111, E05002.
- Hinson, D.P., Wang, H., 2010. Further observations of regional dust storms and baroclinic eddies in the northern hemisphere of Mars. *Icarus* 206, 290–305.
- Hinson, D.P., Wilson, R.J., 2002. Transient eddies in the southern hemisphere of Mars. *Geophys. Res. Lett.* 29 (7), 1154.
- Hinson, D.P., Simpson, R.A., Twicken, J.D., Tyler, G.L., Flasar, F.M., 1999. Initial results from radio occultation measurements with Mars Global Surveyor. *J. Geophys. Res. (Planets)* 104 (E11), 26997–27012.
- Hollingsworth, J.L. et al., 1996. Orographic control of storm zones on Mars. *Nature* 380, 413–416.
- Hollingsworth, J.L., Kahre, M.A., 2010. Extratropical cyclones, frontal waves, and Mars dust: Modeling and considerations. *Geophys. Res. Lett.* 37, L22202.
- Hollingsworth, J.L., Haberle, R.M., Schaeffer, J., 1997. Seasonal variations of storm zones on Mars. *Adv. Space Res.* 19 (8), 1237–1240.
- Joshi, M.M., Lewis, S.R., Read, P.L., Catling, D.C., 1994. Western boundary currents in the atmosphere of Mars. *Nature* 367, 548–552.
- Joshi, M.M., Lewis, S.R., Read, P.L., Catling, D.C., 1995. Western boundary currents in the martian atmosphere: Numerical simulations and observational evidence. *J. Geophys. Res.* 100, 5485–5500.
- Lait, L.R., Stanford, J.L., 1988. Applications of asymptotic space-time Fourier transform methods to scanning satellite measurements. *J. Atmos. Sci.* 45, 3784–3799.
- Leovy, C.B., 1981. Observations of martian tides over two annual cycles. *J. Atmos. Sci.* 38, 30–39.
- Leovy, C.B., Zurek, R.W., 1979. Thermal tides and martian dust storms – Direct evidence for coupling. *J. Geophys. Res.* 84, 2956–2968.
- Leovy, C.B., Tillman, J.E., Guest, W.R., Barnes, J.R., 1985. Interannual variability of martian weather. In: Hunt, G.E. (Ed.), *Recent Advances in Planetary Meteorology*. Cambridge University Press, New York, pp. 69–84.
- Lewis, S.R., Montabone, L., Read, P.L., Rogberg, P., Wilson, R.J., Smith, M.D., 2007. Planetary waves in an assimilation of three Mars years of Thermal Emission Spectrometer data from Mars Global Surveyor. *LPI Contrib.* 1353, 3167–3170.
- Lewis, S.R., Montabone, L., Read, P.L., Rogberg, P., Wilson, R.J., Smith, M.D., 2008. Data assimilation of three Mars years of Thermal Emission Spectrometer observations: Large-scale transient and stationary waves. *LPI Contrib.* 1447, 9009–9012.
- Liu, J., Richardson, M.I., Wilson, R.J., 2003. An assessment of the global, seasonal, and interannual spacecraft record of martian climate in the thermal infrared. *J. Geophys. Res. (Planets)* 108 (E8), 5089.
- Malin, M.C., Edgett, K.S., 2001. Mars Global Surveyor Mars Orbiter Camera: Interplanetary cruise through primary mission. *J. Geophys. Res. (Planets)* 106, 23429–23570.
- Malin, M.C., Danielson, G.E., Ingersoll, A.P., Masursky, H., Veverka, J., Ravine, M.A., Soulanille, T.A., 1992. Mars observer camera. *J. Geophys. Res. (Planets)* 97 (E5), 7699–7718.
- Newman, C.E., Lewis, S.R., Read, P.L., Forget, F., 2002. Modeling the martian dust cycle 2. Multiannual radiatively active dust transport simulations. *J. Geophys. Res. (Planets)* 107, 5124.
- Ryan, J.A., Sharman, R.D., 1981. Two major dust storms, one Mars year apart – Comparison from Viking data. *J. Geophys. Res.* 86, 3247–3254.
- Ryan, J.A., Henry, R.M., Hess, S.L., Leovy, C.B., Tillman, J.E., Walcek, C., 1978. Mars meteorology – Three seasons at the surface. *Geophys. Res. Lett.* 5, 715–718.
- Salby, M.L., 1982a. Sampling theory for asymptotic satellite observations. Part I: Space-time spectra, resolution, and aliasing. *J. Atmos. Sci.* 39, 2577–2600.
- Salby, M.L., 1982b. Sampling theory for asymptotic satellite observations. Part II: Fast Fourier synoptic mapping. *J. Atmos. Sci.* 39, 2601–2614.
- Smith, M.D., 2004. Interannual variability in TES atmospheric observations of Mars during 1999–2003. *Icarus* 167, 148–165.
- Smith, M.D., 2009. THEMIS observations of Mars aerosol optical depth from 2002–2008. *Icarus* 202, 444–452.
- Smith, M.D., Conrath, B.J., Pearl, J.C., Christensen, P.R., 2002. Thermal Emission Spectrometer observations of martian planet-encircling dust storm 2001A. *Icarus* 157, 259–263.
- Strausberg, M.J., Wang, H., Richardson, M.I., Ewald, S.P., Toigo, A.D., 2005. Observations of the initiation and evolution of the 2001 Mars global dust storm. *J. Geophys. Res. (Planets)* 110 (E9), E02006.
- Wang, H., 2007. Dust storms originating in the northern hemisphere during the third mapping year of Mars Global Surveyor. *Icarus* 189, 325–343.
- Wang, H., Ingersoll, A.P., 2002. Martian clouds observed by Mars Global Surveyor Mars Orbiter Camera. *J. Geophys. Res. (Planets)* 107 (E10), 5078.
- Wang, H., Richardson, M.I., Wilson, R.J., Ingersoll, A.P., Toigo, A.D., Zurek, R.W., 2003. Cyclones, tides, and the origin of a cross-equatorial dust storm on Mars. *Geophys. Res. Lett.* 30 (9), 1488.
- Wang, H., Zurek, R.W., Richardson, M.I., 2005. Relationship between frontal dust storms and transient eddy activity in the northern hemisphere of Mars as observed by Mars Global Surveyor. *J. Geophys. Res. (Planets)* 110 (E9), E07005.
- Wilson, R.J., Hamilton, K., 1996. Comprehensive model simulation of thermal tides in the martian atmosphere. *J. Atmos. Sci.* 53, 1290–1326.
- Wilson, R.J., Banfield, D., Conrath, B.J., Smith, M.D., 2002. Traveling waves in the northern hemisphere of Mars. *Geophys. Res. Lett.* 29 (14), 1684.
- Wilson, R.J., Hinson, D., Smith, M.D., 2006. GCM simulations of transient eddies and frontal systems in the martian atmosphere. In: Forget, F., Lopez-Valverde, M.A., Desjean, M.C., Huot, J.P., Lefevre, F., Lebonnois, S., et al. (Eds.), *Mars Atmosphere Modelling and Observations*. pp. 154–158.
- Wu, D.L., Hays, P.B., Skinner, W.R., 1995. A least squares method for spectral analysis of space-time series. *J. Atmos. Sci.* 52, 3501–3511.
- Zurek, R.W., Leovy, C.B., 1981. Thermal tides in the dusty martian atmosphere – A verification of the theory. *Science* 213, 437–439.
- Zurek, R.W., Barnes, J.R., Haberle, R.M., Pollack, J.B., Tillman, J.E., Leovy, C.B., 1992. Dynamics of the atmosphere of Mars. In: Kieffer, H.H., Jakosky, B.M., Snyder, C.W., Matthews, M.S. (Eds.), *Mars. Univ. of Arizona Press, Tucson*, pp. 835–933.